Journal of Catalysis **188,** 311–324 (1999)
Article ID jcat.1999.2625, available online at http://www.idealibrary.com on IDEAL®

Preparation and Activity of Cu–Al Mixed Oxides via Hydrotalcite-like Precursors for the Oxidation of Phenol Aqueous Solutions

A. Alejandre,* F. Medina,*,[1] X. Rodriguez,* P. Salagre,† and J. E. Sueiras*

*Departament d'Enginyeria Química, ETSEQ, Universitat Rovira i Virgili, Pl. Imperial Tarraco 1, 43005 Tarragona, Spain; †Facultat de Química, Universitat Rovira i Virgili, Pl. Imperial Tarraco 1, 43005 Tarragona, Spain

Received April 26, 1999; revised July 5, 1999; accepted July 7, 1999

We performed thermogravimetric analysis (TGA), X-ray diffraction (XRD), BET areas, and FT-IR spectroscopy to characterize copper–aluminium mixed-oxide samples with Cu/Al ratios between 0.5 and 3.0. The thermal stability, crystallinity, and purity of the materials depended on the Cu/Al atomic ratio. The FT-IR and TG detected carbonate (mainly) and nitrate as counteranions which interact in the interlayer region. We found loosely bound carbonate and nitrate anions and one strongly bound type of carbonate. We used dynamic XRD experiments to study the evolution of phases during calcination. All the samples after calcination showed well-dispersed CuO and/or $CuAl_2O_4$ phases. We also tested their catalytic behaviour for the oxidation of 5 g/l phenol aqueous solutions using a triphasic tubular reactor working in a trickle-bed regime and air with an oxygen partial pressure of 0.9 MPa at a temperature reaction of 413 K. Phenol conversion decreased continuously over time for the samples calcined at lower temperatures (673 K). This is because of continuous loss of the CuO phase by elution and the formation of a new phase like copper oxalate on the surface of the copper catalysts which also elutes with time XRD shows that samples calcined at higher temperatures (1073 K) and after HCl treatment (0.1 M) to avoid the CuO phase, have a pure copper aluminate phase. This $CuAl_2O_4$ phase reaches steady activity plateaus in the 55–65% range of phenol conversion. The triphasic tubular reactor using trickle-bed regime largely avoids polymer formation as a catalyst-deactivation process.

Key Words: **copper hydrotalcite-like compounds; copper aluminate; phenol oxidation.**

INTRODUCTION

Hydrotalcite-like materials (HT) belonging to the class of anionic clays have a brucite-like $Mg(OH)_2$ network in which an isomorphous substitution of Mg^{2+} by a trivalent element M^{3+} occurs. The structure of the hydrotalcite is very similar to that of brucite. In brucite, each magnesium cation is octahedrally surrounded by hydroxyls. The resulting octahedron shares edges to form infinite sheets having no net charge.

When Mg^{2+} ions are replaced by a trivalent ion (which, like Al^{3+}, does not have too different a radius), a positive charge is generated in the brucite sheet. The positively charged Mg–Al double hydroxide sheets (or layers) are charge-balanced by the carbonate anions residing in the interlayer sections of the clay structure. In the free space of this interlayer the water of crystallization also finds a place (1–5). The hydrotalcite-like compounds are generally described by the empirical formula

$$\left[(M^{2+})_n(M^{3+})_m(\mathrm{OH})_{2(n+m)}\right]^{m+}\left[(A^{x-})_{m/x}\cdot y\mathrm{H_2O}\right],$$

where M^{2+} and M^{3+} are metal cations, A represents the x-valent anion needed to compensate the net positive charge, x is the charge of the anion, the $m/(m+n)$ ratio may vary from 0.17 to 0.33 depending on the particular combination of di- and trivalent elements, and y is the number of interlayer water molecules. The hydrotalcite and hydrotalcite-like structure is schematically represented in Fig. 1.

Anionic clays based on HT have many practical applications, such as catalysts, catalyst supports, ion exchangers, stabilisers, and adsorbents, mainly because of their variable chemical compositions and recently, they have been among the most widely investigated catalyst precursors because of the remarkable properties of the final catalysts. These include a large surface area, basic properties, high metal dispersion, and stability against sintering even under extreme conditions (6–15). Furthermore, all the divalent metals from Mg^{2+} to Mn^{2+} form hydrotalcite-like compounds, except Cu^{2+}, which forms HT only when other bivalent cations such as Zn, Cr, Co, Mg, and Mn are present (13–15).

An amorphous CuAl-HT can be prepared by decomposing a copper ammoniacal complex on γ-Al_2O_3 (16). Reichle and co-workers (17–18) report the formation of $CuAlCO_3$-HT when the gel obtained by using aqueous solutions of bicarbonate as a precipitant is crystallized at relatively high temperatures.

CuAl-HT are always mixed with other phases, such as malachite or gerhardtite, due to the Jahn–Teller effect of the Cu^{2+} ion (17–22).

[1] To whom correspondence should be addressed.

0021-9517/99 $30.00

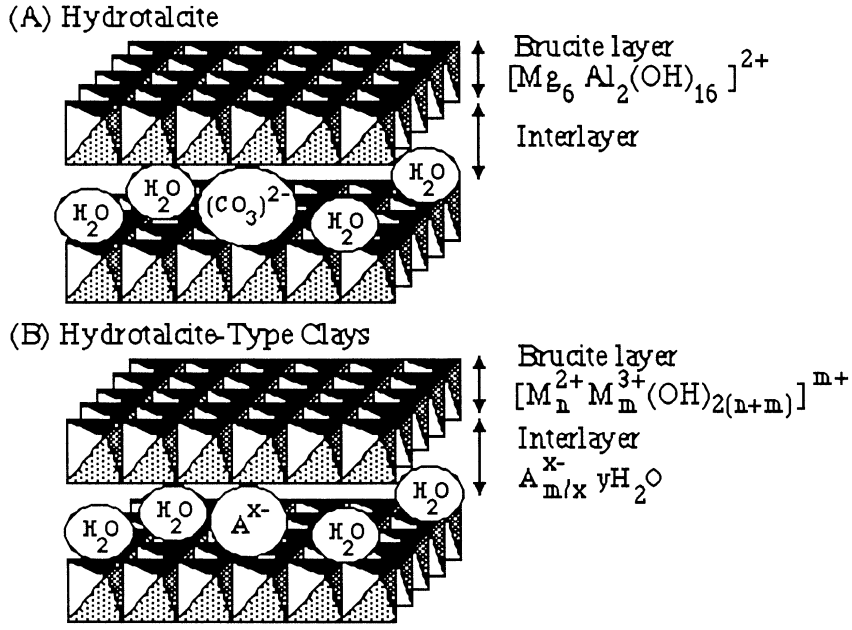

FIG. 1. Schematic presentation of (A) hydrotalcite and (B) hydrotalcite-like materials.

Yamaoka *et al.* (19) noticed that $Na_2Al_2(CO_3)_2 \times 2.9H_2O$ mixed with HT is obtained when Na_2CO_3 is used as a precipitant. Calcination of the latter leads to $NaAlO_2$, which competes with the formation of $CuAl_2O_4$.

Moreover, supported metal oxide catalysts are widely used in oxidation processes. The oxidation of dilute aqueous solutions for organic pollutants using air or oxygen over a solid catalyst is a useful and inexpensive process in which the organic compounds are oxidised to carbon dioxide and water (23–29). Batch and semibatch approaches have previously been studied (23–26).

It has been reported recently (27–30) that continuous processes in a three-phase reactor in a trickle-bed regime are suitable in much milder conditions for the catalytic treatment of aqueous solutions with pollutant loading. However, the catalyst that has been used until now, for large run-times (e.g., more than 10 days), suffers a serious loss in activity and deactivation due to the strong oxidation conditions of the processes and the solubilisation of the active phases (27, 30).

Mixed oxides crystallizing in the spinel form are potential catalysts for the oxidation of phenol in aqueous solutions due to their stability at these reaction conditions (30). The activity of these catalysts can be related to the BET area of the spinel form (31). This paper studies the catalytic behaviour of several copper–aluminium mixed-oxide samples with high BET areas, using copper hydrotalcite-like phases as precursors for the oxidation of 5 g/l phenol aqueous solutions in a triphasic tubular reactor working in a trickle-bed regime. We also study the nature and characteristics of these copper hydrotalcite-like compounds and the chemical changes which take place before the spinel phases are formed.

EXPERIMENTAL

Sample Preparation

Four samples of copper–aluminium hydrotalcite-like compounds were synthesized with Cu/Al ratios of 0.5, 1.0, 2.0, and 3.0. They were obtained by coprecipitation from two aqueous solutions at constant pH between 8 and 8.5 ± 0.2. One of them contained appropriate amounts of $Cu(NO_3)_2 \times 6H_2O$ and $Al(NO_3)_3 \times 9H_2O$ (e.g., 0.2 mol/0.4 mol, 0.2 mol/0.2 mol, 0.2 mol/0.1 mol, and 0.3 mol/0.1 mol of $Cu(NO_3)_2 \times 6H_2O$ and $Al(NO_3)_3 \times 9H_2O$, respectively, dissolved in 400 cm^3 of water) and the other an aqueous solution containing triethylamine (1 M). The two solutions were mixed in a glass reaction vessel (volume 3000 cm^3) initially containing deionised water (200 cm^3). The addition was completed in 3 h under vigorous stirring. During the coprecipitation process, a constant flow of CO_2 was bubbled through the glass reaction vessel. This led to the formation of the carbonate anions in the interlayer region of the solids.

The aqueous solution of triethylamine was used as precipitant rather than ammonia or a sodium base to prevent the formation of the copper–ammonia complex and sodium compounds, respectively. The precipitated gel was aged for 30 min, kept at 313 K. It was then filtered, washed several times with warm distilled water, and then dried in a vacuum at room temperature for 48 h. The calcination process between 393 and 1273 K was performed with a heating rate

of 1 K/min in air and the final calcination temperature was maintained for 16 h.

The copper–aluminium samples obtained in this way are written as HT*N* and their calcined samples are labelled HT*N*(*K*), where *N* is the Cu/Al atomic ratio and *K* the calcination temperature in degrees K. For example, copper–aluminium hydrotalcite with a Cu/Al atomic ratio of 0.5 will be written as HT 0.5 and the corresponding calcined sample at 393 K, as HT 0.5(393). The Cu/Al contents in the coprecipitates were determined using a JEOL 2000FXII equipped with a LINK probe for EDS analysis and atomic absorption spectroscopy (Hitachi Z-8200).

BET Areas

BET surface areas were calculated from the nitrogen adsorption isotherms at 77 K with a Micromeritics ASAP 2000 surface analyser and a value of 0.164 nm^2 for the cross-section of the nitrogen molecule. The same equipment automatically calculates the pore distribution.

X-Ray Diffraction

Powder X-ray diffraction (XRD) patterns of the catalysts were obtained with a Siemens D5000 diffractometer by nickel-filtered Cu $K\alpha$ radiation. The structural evolution during thermal treatment in air was monitored *in situ* with a high temperature XRD attachment. These thermal treatments were performed under flowing air (100 ml/min) from room temperature rising to 1273 K with conditions of sequential temperature increase (2 K/min) and temperature holding time (1 h) before each measurement. The patterns were recorded over a range of 2θ angles from 5° to 85° and compared to the X-ray powder references to confirm phase identities. The patterns of the detected phases were: $Cu_2(OH)_3NO_3$ gerhardtite (JCPDS-ICDD 14-687), $Cu_2(CO_3)(OH)_2$ malachite (JCPDS-ICDD 41-1390), $Cu_6Al_2(OH)_{16}\,CO_3 \times 4H_2O$ (JCPDS-ICDD 37-630)], CuO tenorite (JCPDS-ICDD 41-254), $CuAl_2O_4$ (JCPDS-ICDD 33-448), $Al(OH)_3$ gibbsite (JCPDS-ICDD 7-0324), hydrated aluminium oxide boehmite (JCPDS-ICDD 21-1307), and copper oxalate hydrate moolooite (JCPDS-ICDD 21-0297).

FT-IR Spectroscopy

The FT-IR spectra were recorded on a Nicolet 5ZDX Spectrometer in the 4000–400 cm^{-1} wavenumber range using pressed KBr pellets. The quartz cell with KBr windows was connected to a vacuum line (10^{-3}–10^{-6} Torr) for thermal treatment in a controlled atmosphere.

Thermal Analysis

Thermogravimetric analyses (TGA) was carried out on a Perkin–Elmer TGA 7 microbalance with an accuracy of 1 μg and equipped with a 272–1273 K programmable temperature furnace. Samples of 25 mg were heated at 5 K/min up to 1173 K in a flow of dry helium (80 ml/min). The nature of the gases evolved during the thermal decomposition process was monitored with a QTMD FISONS mass spectrometer.

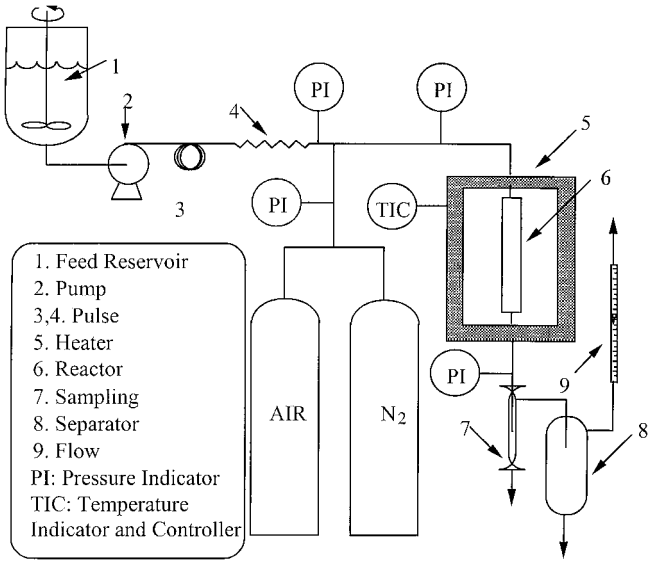

FIG. 2. Experimental setup for catalytic oxidation studies.

Catalytic Measurements

The experimental setup (see Fig. 2) consisted of a stirred, 1-l tank connected to a high-pressure metering pump that works in a flow-rate range of 10–150 ml/h. This pump feeds a triphasic tubular reactor (1.1 cm internal diameter and 20 cm long) operating in a trickle-bed regime and heated by an oven equipped with a temperature control system. The reactor was filled with the catalysts, which had been previously ground and sieved in the range of 25–50 mesh.

The air was directly fed in from a regulated gas cylinder after reaching the desired value. The products of the reaction were rapidly cooled before the liquid and gas phases were separated into two vessels, the smallest of which was used for liquid sampling. The gases were measured with a flow-meter that also worked as a gas flow controller. Both the feed and the different reaction products were analysed by high-performance liquid chromatography (Beckman System Gold, HPLC) to determine the phenol conversion and product distribution, using-Spherisorb ODS2 (25×0.4 cm) as a stationary phase and a mixture of 35% methanol (HPLC quality) and 65% of bidistilled water at pH 2.5 with H_2SO_4 as a mobile phase. A UV spectrophotometer at $\lambda = 219$ and 254 nm was used as a detector. The weight percentage of total carbon difference between the feed and the sum of the reaction organic products, determined by HPLC, was assumed to be the CO_2 released by the reaction (27, 29–31). To evaluate the error of this assumption, the expected COD (chemical oxygen demand from

TABLE 1

Specific Surface Area and Average Pore Diameter (APD) for the Samples Calcined at Different Temperatures

	HT 0.5		HT 1.0		HT 2.0		HT 3.0	
Calcination temperatures (K)	BET area (m^2/g)	APD (Å)	BET area (m^2/g)	APD (Å)	BET area (m^2/g)	APD (Å)	BET area (m^2/g)	APD (Å)
393	181	127	97	155	77	137	47	117
473	161	117	108	135	74	127	64	98
673	217	138	98	156	70	158	57	118
873	190	153	92	169	65	159	57	117
923	150	170	83	175	60	166	53	110
1073	53	247	22	177	35	133	22	102
1273	2	—	2	—	2	—	2	—

total organic matter) values from the HPLC results (feed and total reaction organic products) were compared with the experimental COD values determined by the standard method of $Cr_2O_7^{-2}/Cr^{+3}$ reduction and UV-visible spectroscopy determination of Cr^{3+}. The amount of carbon dioxide was also calculated (for one test), by determining the barium carbonate produced when the gas-outlet stream was continuously bubbled into a saturated barium hydroxide solution (26). The deviations with this method were always less than 4%.

The reaction conditions were: reaction temperature 413 K, gas flow-rate 2.3 ml/s, liquid flow-rate 35.4 ml/h working at 0.41 h of inverse WHSV (weight hourly space velocity), the partial oxygen pressure was maintained at 0.9 MPa, the particle diameter of the catalysts was 25–50 mesh, and 14.52 g of the catalyst was loaded into the reactor. The standard tests of diffusional limitations through the catalysts proved the absence of limitations by external and internal mass transfers. For this purpose, several experiments were performed in which the weight of the catalyst was between 5 and 20 g and the particle diameter was in the range of 25–110 mesh, while the residence time (0.41 h) was maintained.

RESULTS AND DISCUSSION

BET Areas

Table 1 shows the results of the BET and porosimetry determinations that include the BET surface areas and the average pore diameters (Å) for the samples calcined a different temperatures between 393 and 1273 K. The composition of the sample and the calcination temperatures have a strong influence on the surface areas. When both the copper concentration of the sample and the calcination temperatures increase, the BET area values decrease.

The samples calcined between 393 and 873 K have the largest surface areas, which corresponds with the disappearance of the HT XRD pattern (12) (see below in XRD). There is a strong decrease in BET area when the samples are calcined at 1273 K. Sample HT 0.5, which shows the presence of gibbsite phase at room temperature, always has the largest surface area at any calcination temperature. The formation of this alumina hydrate phase (gibbsite), instead of the pure hydrotalcite phase, during the coprecipitation process, may be attributed to their lower divalent/trivalent ratio (5).

X-Ray Diffraction of the Samples before Reaction

Figure 3 shows the X-ray powder patterns of the samples at room temperature, while Table 2 shows the *c* parameters, the structural formulae, and the variation of intensity for the (003) reflection of the samples. The *c* parameter of the copper hydrotalcite-like materials has been calculated from the (003) reflection. The Cu/Al atomic ratios of the solids were determided by EDS and atomic absorption spectroscopy. The results obtained from these techniques are very similar and give the Cu/Al atomic ratios 0.49 (HT 0.5), 1.01(HT 1.0), 1.95 (HT 2.0), and 2.97 (HT 3.0), which agree with the expected values. The structural formulae of

TABLE 2

Compositions of the Samples, *c* Parameters, and Intensity Variations for the [003] Reflection

Sample	Composition	*c* (Å)	Intensity (Cps)
HT 0.5	$Cu_{0.33}\ Al_{0.67}\ (OH)_{2.283}\ (NO_3)_{0.067}\ (CO_3)_{0.161} \times 1.88\ H_2O$	23.065	120
HT 1.0	$Cu_{0.50}\ Al_{0.50}\ (OH)_{2.14}\ (NO_3)_{0.05}\ (CO_3)_{0.154} \times 1.29\ H_2O$	22.982	115
HT 2.0	$Cu_{0.66}\ Al_{0.34}\ (OH)_{1.966}\ (NO_3)_{0.027}\ (CO_3)_{0.173} \times 0.78\ H_2O$	22.848	230
HT 3.0	$Cu_{0.748}\ Al_{0.252}\ (OH)_{2.02}\ (NO_3)_{0.01}\ (CO_3)_{0.11} \times 0.58\ H_2O$	22.856	310

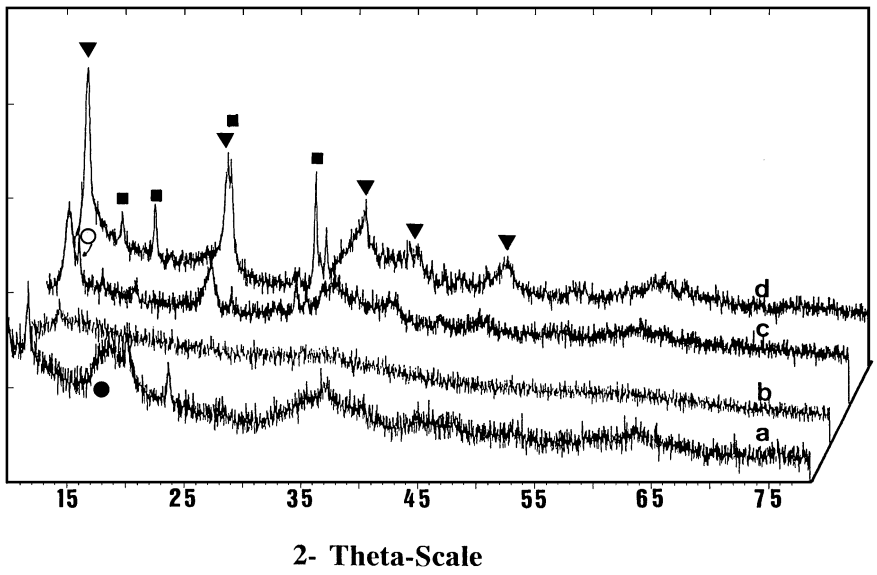

FIG. 3. X-ray diffractograms of noncalcined HT 0.5 (a), HT 1.0 (b), HT 2.0 (c), and HT 3.0 (d) samples. Symbols indicate the presence of copper hydrotalcite (▼), malachite (■), gerhardtite (○), and gibbsite phases (●). The most intense lines of hydrotalcite have been indexed as [003], [006], [012], [015], and [018] for the HT 3.0 (d) sample according to the JCPDS-ICDD 37-630.

the solids were accomplished with thermogravimetric and mass spectra results (see Table 2).

Although a flow of CO_2 was bubbling through the solution during the synthesis of the materials, the coprecipitates contain both nitrate and carbonate as charge-compensating anions.

The following phases were detected: for sample HT 0.5, copper hydrotalcite, malachite, and gibbsite (all these phases had poor crystallinity); for HT 1.0, copper hydrotalcite; for HT 2.0, copper hydrotalcite, malachite, and gerhardtite; and for HT 3.0, copper hydrotalcite and traces of malachite. The most intense diffraction lines for the HT 3.0 sample have been indexed in increasing order of 2θ scale as [003], [006], [012], [015], and [018] in Fig. 3 (according to JCPDS-ICDD 37-630).

Figure 3 shows that essentially amorphous materials are obtained mainly from samples HT 0.5 and HT 1.0. The yield of copper hydrotalcite, which can be correlated with the variations in intensity for the (003) reflection (see Table 2), is higher when the copper content of the sample increases. This agrees with the data reported in the literature that a divalent/trivalent molar ratio equal to or greater than 2.0 is needed to prepare crystallographically pure hydrotalcites (5).

We used Rietveld's method (32) to calculate the amount of hydrotalcite phase in the samples. The results are 10, 25, 55, and 85% for HT 0.5, HT 1.0, HT 2.0, and HT 3.0, respectively. Consequently, the majority of the products obtained from samples HT 0.5 and HT 1.0 were amorphous hydroxide–carbonates (probably also amorphous hydrotalcite-like phases). The HT 1.0 sample is even more poorly crystalline than the HT 0.5 sample. This is probably due to the formation of a gibbsite phase detected by XRD during the coprecipitation of the HT 0.5 sample. The appearance of this side phase (gibbsite) produces an increase of the divalent/trivalent molar ratio for the remaining material, which could promote the formation of more crystalline copper hydrotalcite-like phase.

In all samples there was an increase in malachite and gibbsite phases with a hydrothermal treatment (bubbling CO_2) at 333 K for 48 h (15, 33–35). The copper hydrotalcite phase is therefore destroyed either partially (for HT 2.0 and HT 3.0) or totally (for HT 0.5 and HT 1.0). If the hydrothermal treatment is performed without CO_2, well-crystallised gerhardtite and gibbsite phases are only detected for the HT 0.5 and HT 1.0 samples, and the copper hydrotalcite phase for the HT 2.0 and HT 3.0 samples is also partially destroyed. Therefore, to obtain more copper hydrotalcite phase, ageing processes that improve the more stable phases such as malachite and gerhardtite must be avoided. This behaviour is opposite to that of other hydrotalcite-like compounds, perhaps because, due to the Jahn–Teller effect in the Cu^{2+} ion, the copper hydrotalcite phase is less stable.

To study the transition of copper oxide to copper aluminate phase more accurately, we performed several experiments using a high temperature chamber (HTK Anton Paar) attached to the X-ray diffractometer. These thermal treatments were performed under flowing air (100 ml/min) from room temperature rising to 1273 K with conditions of sequential temperature increase (2 K/min) and temperature holding time (1 h) before each measurement.

The phases detected on heating from 333 to 1273 K are shown in Table 3.

TABLE 3

Crystallite Sizes (Å) and Phases Detected by XRD for the Samples Calcined at Different Temperatures

Calcination temperature (K)	HT 0.5	HT 1.0	HT 2.0	HT 3.0
333	HT Ma Gi	HT	HT(154) Ma Ge	HT(169) Ma
393	HT Ma Gi	—	HT(98) Ma Ge	HT(101) Ma
473	—	CuO(46)	CuO(89) Ma	CuO(80) Ma
673	CuO(35)	CuO(57)	CuO(128)	CuO(120)
873	CuO(45)	CuO(190)	CuO(203)	CuO(198)
923	CuO(60) $CuAl_2O_4$(60)	CuO(220)	CuO(280)	CuO(290)
1073	CuO(45) $CuAl_2O_4$(184)	CuO(258) $CuAl_2O_4$(198)	CuO(332)	CuO(350)
1273	CuO(60) $CuAl_2O_4$(513)	CuO(478) $CuAl_2O_4$(532)	CuO(468) $CuAl_2O_4$(491)	CuO(552) $CuAl_2O_4$(484)

Note. HT, copper aluminium carbonate hydroxide hydrate; Ma, malachite; Gi, gibbsite; Ge, gerhardtite.

The formation of metastable phases from copper hydrotalcite during the calcination process was not detected. This contrasts with the data reported for the Mg/Al hydrotalcite phase (36).

Heating at temperatures above 473 K causes copper hydrotalcite, malachite, and gerhardtite phases to decompose. On the other hand, Mg/Al/CO_3-hydrotalcite phase is stable at temperatures above 650 K (5).

When the HT 0.5–HT 3.0 samples are calcined between 473 and 673 K there is an incipient CuO phase, with the smallest crystals at a lower Cu/Al ratio. An incipient tenorite phase (CuO) is detected for sample HT 0.5 (which has the lowest Cu/Al atomic ratio) at calcination temperatures above 473 K. Moreover, for this sample, which has the same Cu/Al atomic ratio as the stoichiometric copper aluminate, the mainly amorphous CuO phase turns into a well-crystallised and nearly pure copper aluminate at lower calcination temperatures (923 K).

Samples HT 2.0 and HT 3.0, which have the highest Cu/Al atomic ratios, have a well-crystallised CuO phase at temperatures above 473 K. The intensities of the characteristic CuO diffraction lines increase between 473 and 873 K, as the copper content increases. This CuO phase appears together with the copper aluminate phase at higher calcination temperatures (>923 K) (see Table 3).

The CuO and $CuAl_2O_4$ crystallite sizes (calculated from the Sherrer equation) of the samples calcined at different temperatures are also summarised in Table 3. CuO and $CuAl_2O_4$ particles were between 3.5 and 55 and 6 and 53 nm, respectively, at the different calcination temperatures tested. Table 3 shows that particles of CuO and $CuAl_2O_4$ are larger when both the Cu/Al atomic ratio and the calcination temperature increase.

It should be noted that the copper aluminate begins to form at a temperature below 923 K for sample HT 0.5, which agrees with the literature (37, 38), while for sample HT 3.0, which has the highest copper content, it begins to form at about 1223 K.

However, when all samples were calcined at 950 K for 24 h a copper aluminate phase is formed, while for the dynamic XRD experiments a temperature of 1273 K is needed for the HT 3.0 sample to obtain this copper aluminate phase (see Table 3). The rate of formation of copper aluminate is therefore strongly influenced by the amount of copper in the sample, possibly because of the formation of copper aluminate by a solid-state reaction. Larger copper oxide particles (see Table 3) may impede the diffusion of the ions and decrease the rate of formation of the spinel phase (39–41).

FT-IR Spectroscopy

Figure 4 shows the FT-IR spectra of the samples calcined at different temperatures between 333 and 1273 K from precursors HT 0.5 and HT 3.0.

The FT-IR spectra show a band at 3300–3800 cm^{-1} for the samples calcined at lower temperatures, which may be assigned to the stretching mode of hydrogen-bonded hydroxyl groups from the gibbsite and brucite-like layers and from the interlayer water molecules. The breadth of the band increases because it overlaps with a shoulder above 3000 cm^{-1} assigned to ν_{OH} of water molecules hydrogen-bonded to carbonate ions in the interlamellar layer (5, 6,

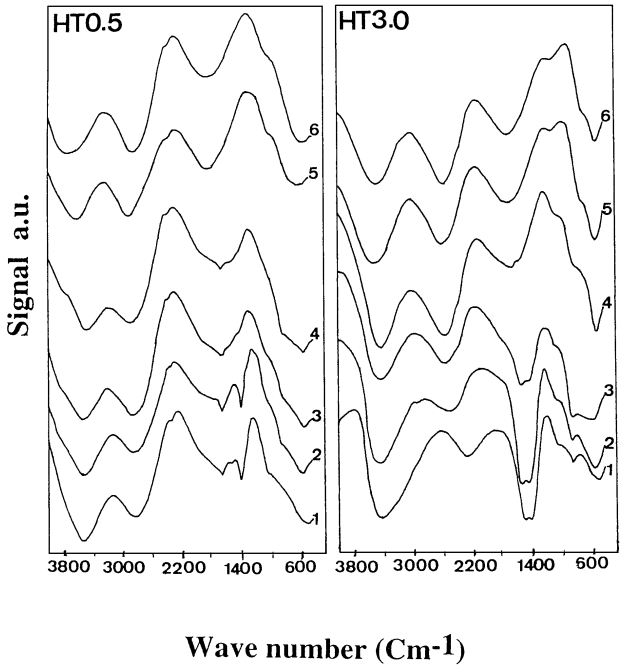

FIG. 4. IR spectra of samples HT 0.5 and HT 3.0, respectively, calcined at different temperatures: (1) $T = 333$ K; (2) $T = 473$ K; (3) $T = 673$ K; (4) $T = 873$ K; (5) $T = 1073$ K, and (6) $T = 1273$ K.

33, 34, 42, 43). Consequently, this band is much broader when the samples contain a higher amount of carbonate. It seems that the carbonate content increases when the Cu/Al atomic ratio in the sample is higher (HT 1.0, HT 2.0, and HT 3.0) than when they do not (HT 0.5), in agreement with the chemical analysis (see Table 2). Also, the position of this band shifts to the region of higher frequency when there is more aluminum in the sample.

Also, the water deformation band is recorded around 1600 cm^{-1}, which overlaps with a double band at about 1350–1500 cm^{-1} for samples HT 1.0 HT 2.0, and HT 3.0 but not for sample HT 0.5, when they are calcined at lower temperatures. This double band could be assigned to the carbonate and nitrate anions in the interlayer of the hydrotalcite-like compounds (19) and possibly by the carbonate anions from the traces of malachite phase detected in samples HT 2.0 and HT 3.0.

On the other hand, only a weak peak is detected around 1350–1390 cm^{-1} for HT 0.5 (which has the highest amount of nitrate anions). This is also probably due to the nitrate and carbonate anions (44).

It is well known that the three IR active absorption bands from the carbonate anion are detected at 1350–1380 cm^{-1}, 850–880 cm^{-1}, and 670–690 cm^{-1}.

Also, the ν_3 vibration of the nitrate anion is detected around 1376 cm^{-1} (44).

However, the double band detected at 1350–1500 cm^{-1} may be attributed either to a lower symmetry of the carbonate and nitrate anions from D_{3h} to C_{2v} in the interlayer or to the disordered nature of the interlayer (34, 35).

When the Cu/Al atomic ratios in the samples increase (in parallel with the increase in hydrotalcite phase), the intensity of this double band increases. These samples also have more carbonate anions (see Table 2). This double band also becomes much weaker when the calcination temperature increases.

Calcination temperatures above 800 K are required to remove this double band from the samples which have a higher copper content.

Furthermore, the peak around 1500 cm^{-1} is more stable at a higher temperature than the peak around 1380 cm^{-1}. We can conclude, therefore, that the rise in the Cu/Al atomic ratio increases the amount of carbonate anions in the interlayer and leads to different types of carbonate sites which have different interactions in the brucite-like layer.

Thermal Analysis

Figure 5 shows the TG diagrams for the four uncalcined samples. There was a considerable weight loss (≈40%) between 400 and 600 K during the thermal decomposition of the HT 0.5 sample and a small loss (≈2%) at about 730 K. The weight loss between 400 and 600 K was also recorded for the other samples but always showed lower weight losses (≈25–33%). New weight losses were detected at higher decomposition temperatures (800–1000 K) when the copper contents in the sample increased (HT 1.0, HT 2.0, and HT 3.0). The changes in weight for these samples at higher temperatures are between 8 and 12%, and the total weight loss during the calcination process was around 40% for the four samples. However, there is a slight decrease in total weight loss when the copper content in the sample increases.

The nature of the gases released during the thermal treatment was monitored by mass spectrometry following the masses 18,17 (H_2O); 30,14 (NO); 30,46 (NO_2); and 44,28 (CO_2). Figure 6 shows the evolution of the species released during the calcination process for the HT 0.5, HT 1.0, HT 2.0, and HT 3.0 noncalcined samples. The behaviour of a pure malachite phase is also shown in Fig. 6e as a reference.

The main species detected by mass spectrometry during the decomposition process were H_2O, CO_2, NO_2, and NO for all the samples. However, when the copper contents increase there is more carbonate in the sample, in agreement with Table 2.

A band of water is detected between 400 and 800 K for the samples. The water loss at lower temperature (380–500 K) is mainly due to the removal of weakly bonded water, which is probably the hydration water located in the interlayer space of the copper hydrotalcite phase. This process is accompanied by the removal of traces of gases such as CO_2, NO_2, and NO. These gases are probably produced by the decomposition of weakly bonded carbonate and nitrate anions, located at the end of the interlayer space (10).

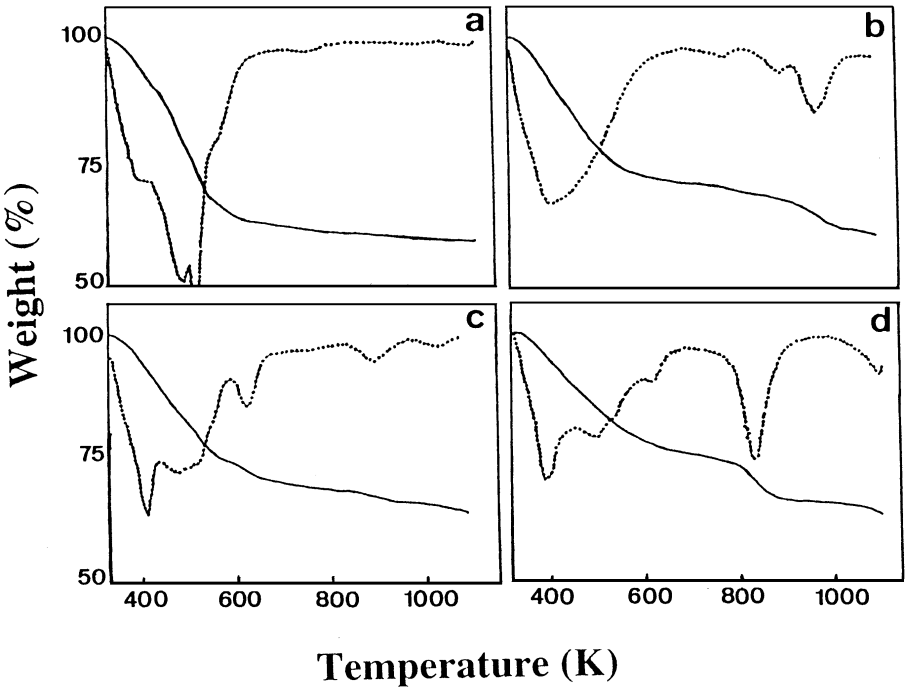

FIG. 5. Weight decrease versus temperature for the thermal decomposition of samples: HT 0.5 (a), HT 1.0 (b), HT 2.0 (c), and HT 3.0 (d).

Furthermore, there was a second loss of water, which always overlapped with the first loss of water, between 500 and 700 K, depending on the copper content of the sample. This second water loss is also accompanied by the removal of NO, NO_2, and CO_2. The weight loss detected for samples HT 1.0 and HT 3.0 between 800 and 1000 K is mainly due to new CO_2 emissions, and this agrees with the data in the literature (45). The emission of CO_2 at a higher temperature, observed for the copper hydrotalcite-like phase may be explained by the fact that during the thermal decomposition of the samples, there is some type of reaction with the carbonate anions in the interlayer space to form some sort of "oxycarbonates" (45). However, this cannot explain the peak detected by FT-IR around 1500 cm^{-1} at room or lower calcination temperatures for the samples with higher Cu/Al atomic ratios.

The CO_2 emission processes of the samples are probably better explained by two different types of carbonate coordinations in the brucite-like layer. The carbonate anion can behave as a monodentate or bidentate ligand in the interlayer region (46).

The monodentate carbonate decomposes at a lower temperature, whereas the bidentate carbonate is more stable at higher temperatures. This mechanism explains the splitting of the bands detected by FT-IR about 1350–1500 cm^{-1} for the samples with higher copper contents.

We suggest, therefore, that this bidentate carbonate, which decomposes at temperatures above 800 K, is probably responsible for the peak detected by FT-IR around 1500 cm^{-1}.

Catalytic Activities

Noncalcined hydrotalcite-like samples show practically no conversion for the catalytic oxidation of phenol in aqueous solutions under the conditions given in the experimental section. Figure 7 shows the conversion during a 30-day run for the samples calcined at 673 K. As we can see, all the catalysts, after the beginning of the reaction (first 40 h), show a more or less constant decrease in phenol conversion from 95 to 0% in ca. 20–30 days. Figure 8 shows the main reaction products for the sample HT 0.5 calcined at 673 K, without taking into account the CO_2 obtained. The activity loss of the catalysts causes a constant decrease in the amount of reaction products. These products are the following (in decreasing order of concentration): oxalic acid, *p*-benzoquinone, formic acid, acetic acid, succinic acid, and catechol. Traces of malonic, acrylic, and fumaric acids are also obtained.

Therefore, the reaction products for all the catalysts are CO_2 (>70%), diphenols, quinones, and organic acids (oxalic, formic, acetic, succinic, etc.). Figure 9 shows a simplified reaction pathway for the phenol oxidation reaction (26).

However, the conversion of the catalysts decreases with run-time and conversion is null for runs up to 20–30 days. In an attempt to explain this activity loss, we studied the possibility of polymer formation using a trickle-bed regime by solid ^{13}C NMR and by both thermal decomposition and combustion with a mass spectrometer detector (see Fig. 10).

It is known that polymers may form during the phenol oxidation reaction by two different reactions which take

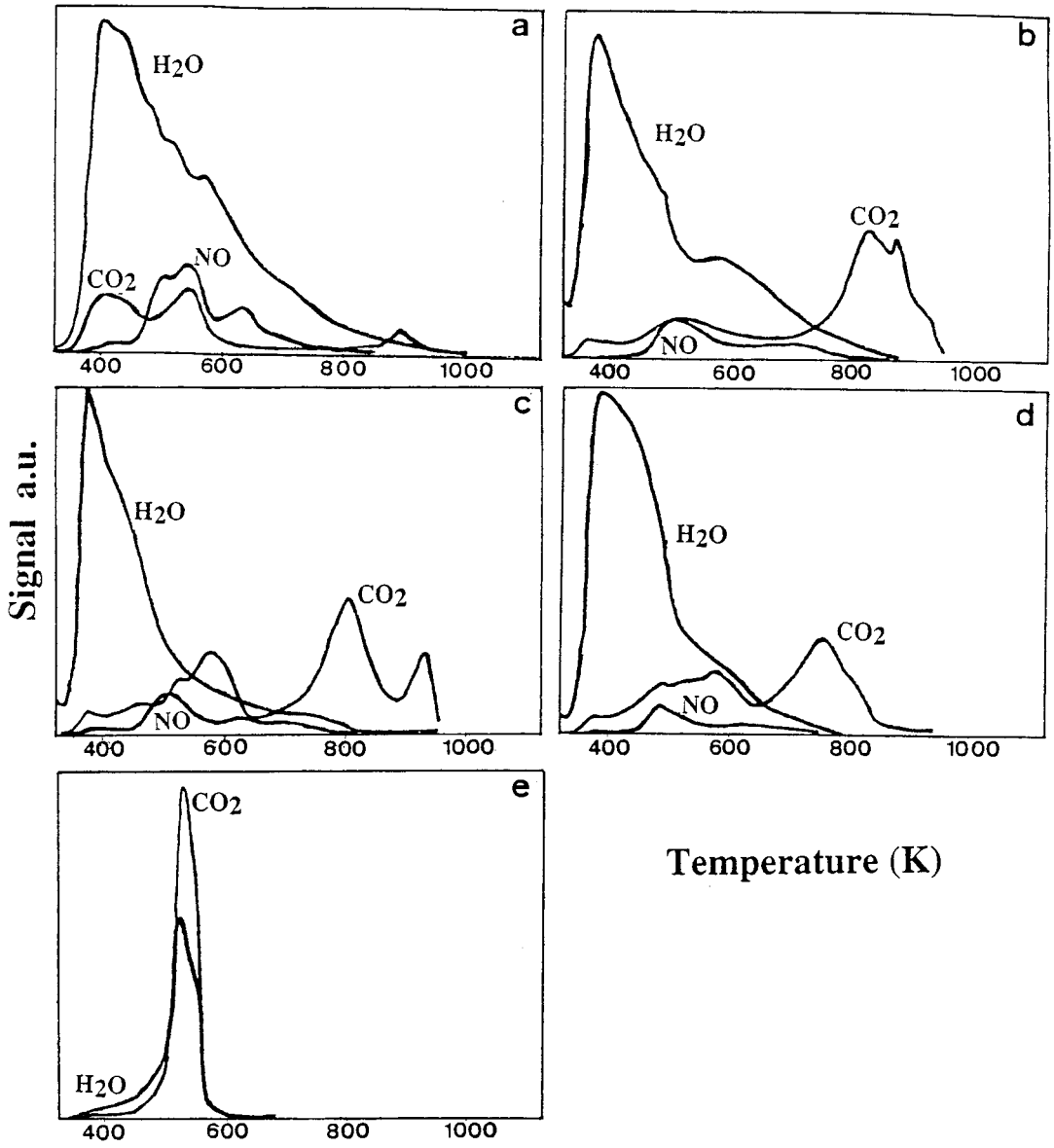

FIG. 6. Thermal decomposition versus temperature performed in an ultrahigh vacuum mass spectrometer for the samples: HT 0.5 (a), HT 1.0 (b), HT 2.0 (c), HT 3.0 (d), and a malachite sample as reference (e).

place in the liquid phase: the addition of glyoxal to phenol or the polymerization of glyoxal (C2 aldehyde) (26). This homogeneous polymerization reaction markedly reduces the level of total phenol oxidation and deactivates the catalyst.

The ^{13}C NMR technique shows no signal between 0 and 300 ppm, even after a time interval of 50 h.

Figure 10B shows only a peak of carbonaceous origin at the CO_2 mass position when a used catalyst (HT 0.5 sample calcined at 673 K during 5-day run) thermally decomposes under helium flow. In theory, this peak may be caused by the copper oxalate which was observed by XRD being formed during the reaction process. After thermal decomposition, the same sample was submitted to an ulterior combustion treatment under O_2 flow and the baseline obtained from the mass run between 2 and 200 mass units was flat (see Fig. 10A). Figure 10C shows the mass-monitored thermal decomposition vs temperature of a fresh HT 0.5 sample calcined at 673 K. This had previously been treated with a hot aqueous solution of oxalic acid for 24 h for the expected formation of copper oxalate. This mass spectrum matches with that obtained in Fig. 10B. Consequently, the results from Fig. 10 confirm the absence of both polymers and coke formations on the surface of the catalysts. This contrasts with the data in the literature when other reactors were used (24, 26), but agrees with runs conducted in a differentially

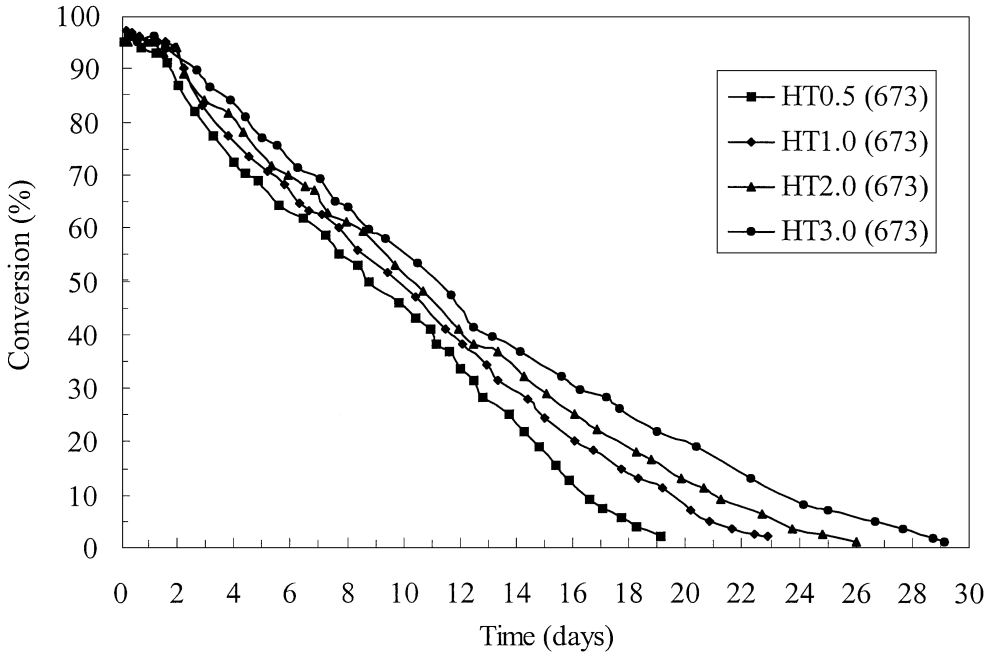

FIG. 7. Evolution of the phenol conversion for the samples HT 0.5–HT 3.0 calcined at 673 K.

operated fixed-bed reactor (47). This may be because of the high solid-to-liquid phase ratio characteristic of a trickle-bed regime, which prevents the formation of polymers (31).

Therefore, when a trickle-bed reactor is used, the activity loss detected for the copper hydrotalcite-like samples calcined at 673 K cannot be explained by the formation of polymers which might cause a poisoning effect on the catalytic sites.

The evolution of the samples calcined at 673 K at different reaction times was observed by XRD. The results are shown in Table 4. Obviously, the crystal phases of the catalysts change quite considerably before, during, and after the reaction. Samples HT 0.5 and HT 1.0 show tenorite (CuO) before reaction, tenorite, moolooite ($CuC_2O_4 \times nH_2O$), and boehmite (AlOOH) during the reaction, and only boehmite after the reaction (20–30 days). Samples HT 2.0 and HT 3.0 behave in a similar way (where the formation of copper hydrotalcite-like phase was also detected). The layered structure is therefore recovered again, probably due to the run conditions (hot water and CO_2 produced

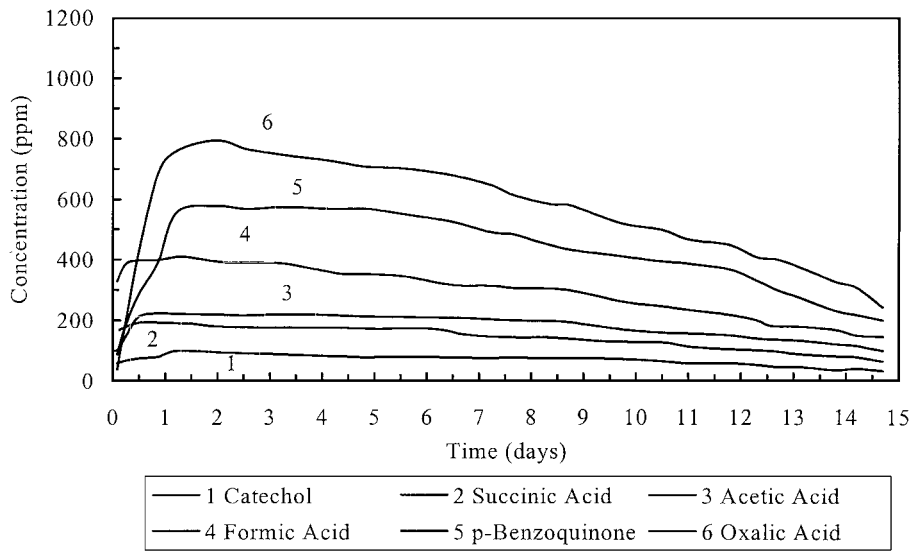

FIG. 8. Plot of the main products for the HT 0.5 sample calcined at 673 K, without taking into account the CO_2 obtained.

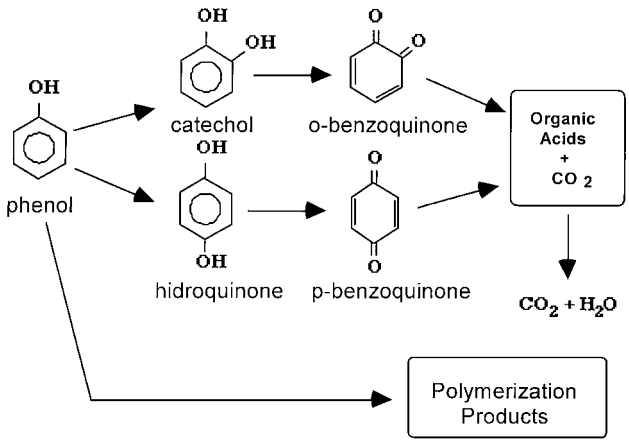

FIG. 9. Simplified reaction pathway of the phenol oxidation reaction.

during the reaction). This reversible behaviour also agrees with other results reported in the literature (8, 9, 48, 49).

Under the reaction condition, the CuO phase, obtained by calcining the copper hydrotalcite-like phase at 673 K, therefore disappears with time.

TABLE 4

XRD Characterisation of Copper Hydrotalcite-like Samples Calcined at 673 K

Sample	XRD phases detected		
	Before reaction	During reaction	After reaction (null conversion)
HT 0.5(673)	T	M, T, B	B
HT 1.0(673)	T	M, T, B	B
HT 2.0(673)	T	HT, M, T, B	B
HT 3.0(673)	T	HT, M, T, B	B

Note. T, tenorite (CuO); M, moolooite ($CuC_2O_4 \times nH_2O$); HT, copper aluminium carbonate hydroxide hydrate; B, bohemite (AlOOH).

Figure 11 illustrates the Cu^{2+} concentration in the outlet stream from the reactor throughout the activity test for sample HT 0.5 calcined at 673 and 1073 K. It shows that solubilisation of the copper oxide for sample HT 0.5(673) increases to a maximum value of around 70 ppm after ca. 24 h and then the concentration of solubilised copper decreases slightly.

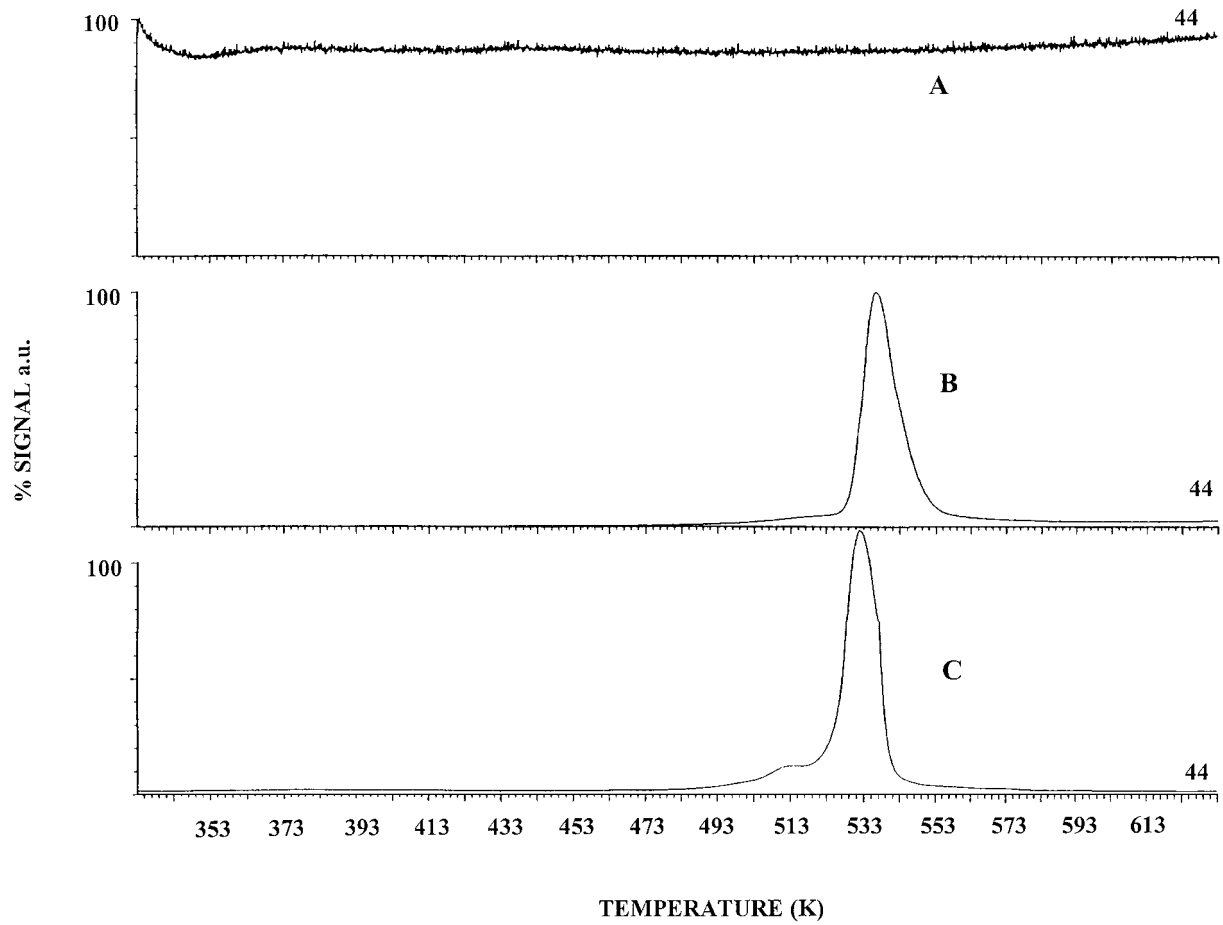

FIG. 10. Thermal decomposition mass spectra of carbon dioxide, at 44 mass atomic units: (B) spent catalyst HT 0.5 calcined at 673 K under helium flow; (A) after the latter thermal decomposition the same sample was submitted to an ulterior combustion treatment under O_2 flow; and (C) thermal decomposition of the fresh catalyst previously treated with a hot aqueous solution of oxalic acid for 24 h for the expected formation of copper oxalate.

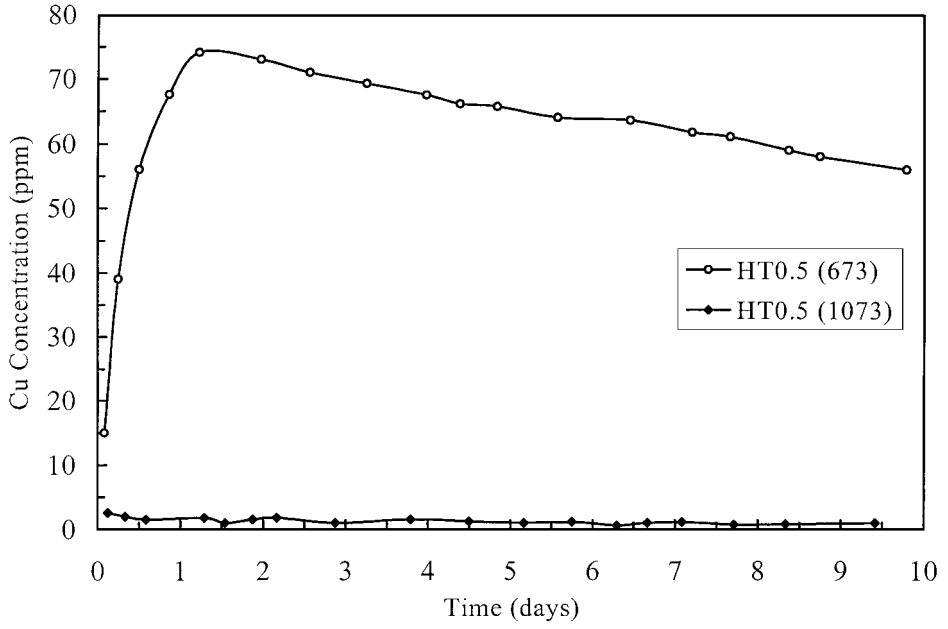

FIG. 11. Cu^{2+} concentration profile during the reaction process for the HT 0.5 sample calcined at 673 and 1273 K.

The loss of copper is due to the effect of the hot acidic aqueous solution from the reaction process that may promote the solubility of copper oxide. On the other hand, sample HT 0.5 calcined at 1073 K shows a loss of copper which is always lower than 3 ppm. These effects are corroborated by XRD.

The rate of wet-air oxidation of a large number of organic compounds increases when homogeneous catalysis is used (50–52). Copper salts are the most effective of homogeneous catalysts. So, to take into account a possible homogeneous catalysis due to the dissolved copper during the reaction process, we performed several catalytic tests with a concentration range of 10–70 ppm. The conversions were always lower than 6% in the same reaction conditions even with a copper concentration of 70 ppm. The conversion is, therefore, mainly due to the heterogeneously catalysed reaction.

Moreover, a new crystalline phase like copper oxalate (moolooite, $CuC_2O_4 \times nH_2O$) was formed during the reaction (see Table 4). This copper oxalate phase may be formed either by the reaction of the oxalic acid (produced during the reaction) with the copper oxide on the surface of the catalyst or by the precipitation of copper oxalate (if we

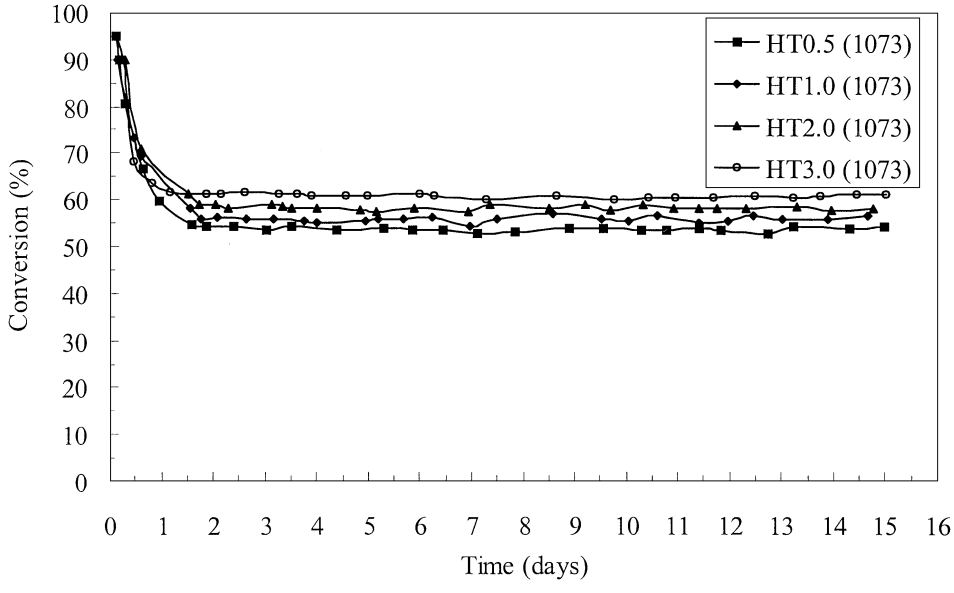

FIG. 12. Evolution of the phenol conversion for the samples HT 0.5–HT 3.0 calcined at 1073 K.

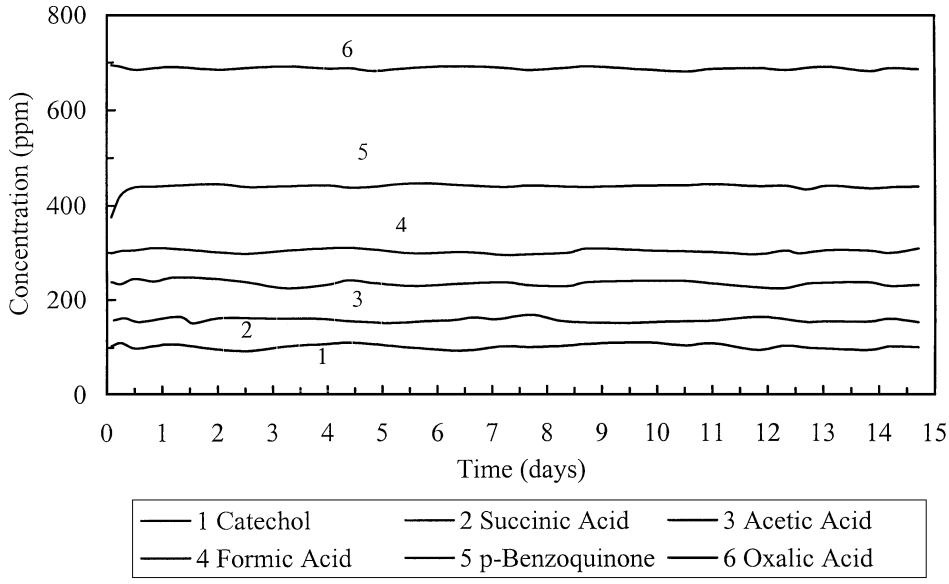

FIG. 13. Plot of the main products for the HT 0.5 sample calcined at 1073 K, without taking into account the CO_2 obtained.

assume that copper ions are obtained from the elution of copper oxide with the organic acids yielded during the process).

When we tested the activity of the copper oxalate supported on alumina, in the same reaction conditions, the conversion was ca. 45% from the beginning, and it gradually decreased with time. These studies suggest, therefore, that copper oxide and copper oxalate are the active phases during the reaction for the hydrotalcite-like samples calcined at 673 K.

Figure 7 shows that when the run-time increases to 20 days, the copper hydrotalcite-like sample HT 0.5 calcined at 673 K has no conversion. However, a run-time of 30 days was needed to obtain null conversion for sample HT 3.0 (which has the highest copper content). So, when the amount of copper oxide increases, the lifetime of the catalysts increases. Moreover, X-ray diffraction of these samples show that boehmite (AlOOH) is the only phase detected after the reaction (see Table 4). Both copper oxide and copper oxalate were therefore dissolved during the reaction time.

Moreover, the four copper hydrotalcite-like samples (HT 0.5–HT 3.0) were calcined at 1073 K for 16 h and their catalytic activities tested. It is important to mention that before the reaction process, all these calcined samples were subjected to HCl treatment (HCl 0.1 M) several times until no elution of copper oxide was detected by atomic absorption spectroscopy. After this treatment, the samples were again calcined at 1073 K for 1 h to remove all the chlorine species. The X-ray diffraction of these samples shows that copper aluminate ($CuAl_2O_4$) is the only phase detected before, during, and after the reaction. Figures 12 and 13 show the conversion during a 15-day run for the four samples and the evolution of the main products obtained during the reaction process for the HT 0.5(1073) sample (without taking into account CO_2 conversion (>80%)), respectively. The main products obtained during the phenol oxidation reaction for the other samples are similar. As we can see, after the beginning of the reaction (first 20 h, the time needed for steady state condition in the reactor), all the catalysts show a more or less constant phenol conversion of around 55% for the HT 0.5 sample and up to 65% for the HT 3.0 sample, under the experimental conditions described in the experimental section. The copper aluminate phase therefore shows higher activity and stability for the oxidation of phenol in aqueous solutions.

CONCLUSIONS

Four copper–aluminium samples with Cu/Al atomic ratios between 0.5 and 3.0 were prepared using trimethylamine and CO_2 as precipitants. Several techniques such as TG, XRD, BET areas, and FT-IR were performed to characterise these solids. The thermal stability, crystallinity, and purity of the materials depended on the Cu/Al atomic ratio added during the coprecipitation process.

The copper hydrotalcite phase was sometimes accompanied by other phases like gibbsite, malachite, and gerhardtite. The copper hydrotalcite phase was stable and purer at high Cu/Al atomic ratios. The FT-IR and TG detected carbonate (mainly) and nitrate as counteranions with different interactions in the interlayer region. There are both loosely bound carbonate and nitrate anions and a strongly bound carbonate that decomposes at higher temperatures. We studied the evolution of the phases obtained during the calcination process by dynamic XRD experiments.

The copper hydrotalcite phase is only stable at calcination temperatures below 500 K. All the samples showed a well-dispersed CuO (at low calcination temperatures) and copper aluminate phase (at higher calcination temperatures).

We also studied the materials obtained by calcination at 673 and 1073 K for 16 h for the oxidation of phenol in aqueous solutions using a trickle-bed reactor. All the catalysts were highly active and they preferentially selected CO_2 during the catalytic phenol oxidation reaction. Conversion of the catalysts from the calcination of the copper hydrotalcite-like materials at lower temperature (673 K) decreased continuously over time. This loss in activity may be explained by the disappearance of copper oxide and copper oxalate, which are dissolved because of the hot acidic medium due to the reaction conditions. On the other hand, conversion of the copper aluminate phase from the calcination of the copper hydrotalcite-like materials at higher temperature (1073 K) was higher for the oxidation of phenol and was stable under the reaction conditions. This may be of interest in oxidation reactions. We also found that the trickle-bed triphasic tubular reactor largely avoided polymer formation as a catalyst deactivation process during the phenol oxidation reaction in aqueous solutions.

REFERENCES

1. Allmann, R., and Lohse, H. H., *N. Jhb. Miner. Mh.* **6**, 161 (1966).
2. Ingram, L., and Jepsen, H. P., *N. Jhb. Miner. Mh.* **36**, 465 (1967).
3. Taylor, H. F. W., *Miner. Mag.* **39**, 377 (1973).
4. Bhattacharyya, A., Chang, V. W., and Shumacher, D. J., *Appl. Clay Sci.* **13**, 317 (1998).
5. Cavani, F., Trifiro, F., and Vaccari, A., *Catal. Today* **11**, 173 (1991).
6. Trifiro, F., and Vaccari, A., *Comprehen. Supramol. Chem.* **7**, 25 (1996).
7. Corma, A., Fornes, V., Martin-Aranda, R. M., and Rey, F., *J. Catal.* **134**, 58 (1992).
8. Climent, M. J., Corma, A., Iborra, S., and Prima, J., *J. Catal.* **151**, 60 (1995).
9. Tichit, D., Lhouty, M. H., Guida, A., Chiche, B. H., Figueras, F., Auroux, A., Bartalini, B., and Garrone, E., *J. Catal.* **151**, 150 (1995).
10. Velu, S., and Swamy, C. S., *Appl. Catal.* **145**, 141 (1996).
11. Medina, F., Tichit, D., Coq, B., Vaccari, A., and Dung, N. T., *J. Catal.* **167**, 142 (1997).
12. Fornasari, G., Gazzano, M., Matteuzzi, D., Trifirò, F., and Vaccari, A., *Appl. Clay Sci.* **10**, 69 (1995).
13. Gusi, S., Pizzoli, F., Trifirò, F., Vaccari, A., and Del Piero, G., *in* "Preparation of Catalysts IV" (B. Delmon, P. Grange, P. A. Jacobs, and G. Poncelet, Eds.), p. 753. Elsevier, Amsterdam, 1987.
14. Doesburg, E. B. M., Höppener, R. H., de Koning, B., Xiaoding, X., and Scholten, J. J. F., *in* "Preparation of Catalysts IV" (B. Delmon, P. Grange, P. A. Jacobs, and G. Poncelet, Eds.), p. 767. Elsevier, Amsterdam, 1987.
15. Busetto, C., Del Piero, G., Manara, G., Trifirò, F., and Vaccari, A., *J. Catal.* **85**, 260 (1984).
16. Herman, R. G., Klier, K., Simmons, G. W., Finn, B. P., and Bulko, J. B., *J. Catal.* **56**, 407 (1979).
17. Reichle, W. T., *J. Catal.* **94**, 547 (1985).
18. Reichle, W. T., Kang, S. Y., and Everhardt, D. S., *J. Catal.* **101**, 352 (1986).
19. Yamaoka, T., Abe, M., and Tsuji, M., *Mater. Res. Bull.* **24**, 1183 (1989).
20. Trifirò, F., Vaccari, A., and Del Piero, G., *Stud. Surf. Sci. Catal.* **39**, 571 (1988).
21. Kannan, S., and Swamy, C. S., *Appl. Catal. B* **3**, 205 (1994).
22. Köckerling, M., Geismar, G., Henkel, G., and Nolting, H. F., *J. Chem. Soc., Faraday Trans.* **93**, 481 (1997).
23. Sadana, A., and Katzer, J., *J. Catal.* **35**, 140 (1974).
24. Ohta, H., and Goto, S., *Ind. Eng. Chem. Fundam.* **19**, 180 (1980).
25. Willms, R. S., Balinski, A. M., Reible, D. D., Wetzel, D. M., and Harrison, D. P., *Ind. Eng. Chem. Res.* **26**, 148 (1987).
26. Pintar, A., and Levec, J., *J. Catal.* **135**, 345 (1992).
27. Fortuny, A., Ferrer, C., Bengoa, C., Font, J., and Fabregat, A., *Catal. Today* **24**, 79 (1995).
28. Pintar, A., and Levec, J., *Catal. Today* **24**, 51 (1995).
29. Alejandre, A., Medina, F., Fortuny, A., Salagre, P., and Sueiras, J. E., *Appl. Catal. B: Environ.* **16**, 53 (1998).
30. Alejandre, A., Medina, F., Fabregat, A., Salagre, P., and Sueiras, J. E., *in* "Proceedings, 3rd World Congress of Oxidation Catalysis. San Diego, 1997," abstracts K-2, September, 1997.
31. Alejandre, A., Medina, F., Fabregat, A., Salagre, P., and Sueiras, J. E., *Appl. Catal. B: Environ.* **18**, 307 (1998).
32. Rietveld, H. A., *J. Appl. Cryst.* **2**, 65 (1969).
33. Roy, A., Forano, C., Malki, D., and Besse, J., *in* "Synthesis of Microporous Materials, V. II, Expanded Clays and Other Microporous Solids" (M. L. Occelli and H. E. Robson, Eds.), p. 108. Van Nostrand–Reinhold, New York, 1992.
34. Bish, D. L., and Brindley, G. W., *Amer. Mineral.* **62**, 458 (1997).
35. Hernandez-Moreno, M. J. H., Ulibarri, M. A., Rendon, J. L., and Serna, J. L., *Phys. Chem. Miner.* **12**, 34 (1985).
36. Kanezaki, E., *Inorg. Chem.* **37**, 2588 (1998).
37. Jacob, K. T., and Alcock, C. B., *J. Am. Ceram. Soc.* **38**(5, 6), 192 (1975).
38. Susnitzky, D. W., and Carter, C. B., *J. Mater. Res.* **6**, 1958 (1991).
39. Shaikhutdinov, S. K., Avdeeva, L. B., Goncharova, O. V., Kochubey, D. I., Novgorodov, B. N., and Plyasova, L. M., *Appl. Catal.* **126**, 125 (1995).
40. Alzamora, L. E., Ross, J. R. H., Druissink, E. C., and van Rejen, L. L., *J. Chem. Soc. Faraday Trans.* **77**, 667 (1981).
41. Zielinski, *J. Appl. Catal. A* **94**, 107, (1993).
42. Kooli, F., Rives, V., and Ulibarri, M. A., *Inorg. Chem.* **34**, 5122 (1995).
43. Kruissink, E. C., Van Reijden, L. L., and Ross, J. R. H., *J. Chem. Soc. Faraday Trans.* **77**, 649 (1981).
44. Velu, S., Ramkumar, V., Narayanan, A., and Swamy, C. S., *J. Mater. Sci.* **32**, 957 (1997).
45. Velu, S., and Swamy, C. S., *J. Mater. Sci. Lett.* **15**, 1674 (1996).
46. Miyata, S., and Okada, A., *Clays Clay Miner.* **25**, 14 (1977).
47. Pintar, A., and Levec, J., "3rd World Congress on Oxidation Catalysis," *Stud. Surf. Sci. Catal.* **110**, 633 (1997).
48. Rey, F., Fornés, V., and Rojo, J. M., *J. Chem. Soc. Faraday Trans.* **88**, 2233 (1992).
49. Constantino, V. R. L., and Pinnavaia, T., *J. Inorg. Chem.* **34**, 883 (1995).
50. Joglekar, H. S., Samant, S. D., and Joshi, J. B., *Water Res.* **25**, 135 (1991).
51. Fajerweg, K., and Debellefontaine, H., *Appl. Catal. B: Environ.* **10**, 229 (1996).
52. Mishra, S. V., Mahajani, V. V., and Joshi, J. B., *Ind. Eng. Chem. Res.* **34**, 2 (1995).